UNIVERSITY of CALIFORNIA
Santa Barbara

Enhanced yield-mobility products in hybrid halide Ruddlesden–Popper compounds with aromatic ammonium spacers

A Thesis submitted in partial satisfaction of the
requirements for the degree
Master of Science
in
Chemistry

by

Brian Barraza

Committee in Charge:

Professor Ram Seshadri, Chair

Professor Trevor Hayton

Professor Javier Read de Alaniz

March 2024

The thesis of Brian Barraza is approved.

_____

Professor Trevor Hayton

_____

Professor Javier Read de Alaniz

_____

Professor Ram Seshadri, Committee Chair

March 2024

Enhanced yield-mobility products in hybrid halide Ruddlesden–Popper compounds with aromatic ammonium spacers

by

Brian Barraza

Del mismo pozo

Acknowledgments

Above all, I would like to express my gratitude to my advisor, Ram Seshadri. I am deeply thankful for his decision to welcome me into his group (twice) and for the support and patience he has shown me over the past decade. Ram's exceptional body of work and his dedication to teaching are clearly powered by his profound appreciation for the intrinsic patterns in these processes, evident in both his acute skill in identifying motifs and the mentorship and support he extends to his students.

I would also like to extend my gratitude to Trevor Hayton and Javier Read de Alaniz for agreeing to serve on my committee at short notice. Despite being some 900 miles away, Trevor's unique approach to scientific inquiry significantly shaped my interest in chemistry. Additionally, I am thankful to Javier; our few but honest conversations stand out as some of the most candid during my time at UCSB. Thank you for that.

Speaking of honest conversations, I would like to express my gratitude to my undergraduate advisor, Skye. I've been fortunate enough to count him among my friends over the passing years. Visits to El Paso are never complete without stopping by his office, unannounced, to share with each other our most recent escapades. Thank you for all the work and effort with me in the lab.

I am immensely grateful to everyone who facilitated my return to UCSB after six years. The journey involved numerous complexities, and I am eternally appreciative of all who contributed to making it possible. Specifically, I would like to extend my heartfelt thanks to a few individuals who played pivotal roles: Iris Chan, the Graduate Program Advisor in the Department of Chemistry and Biochemistry; Zach Cooseboom with Billing Services; Mike Fogelsonger, the Director of Veterans and Military Services; and a very special thanks to my VR&E counselor, Charlee.

A heartfelt thank you to Guang Wu, the Chemistry Department's staff crystallographer, for his contributions to my education. Above all, I am grateful for his unconventional and creative approach to research. Who would have thought that a walk out in nature could lead to better quality crystal data? Dr. Wu, that's who!

Regarding research, I would like to recognize Naveen, Ali, and Emily. These three individuals were not only friends throughout my graduate studies but also played crucial roles in publishing my research efforts during my absence. Naveen and Ali shouldered the majority of the responsibility for publishing this work, while Emily acted as a most skilled translator to my raw data and notes.

During my time at UCSB, I was fortunate to meet many individuals who have become some of my closest friends over the last decade. Ali, Amir, Brett, Danny, Elena, Iana, Jason, Kent, Mikio, Naveen and Rachel, my life would not be the same without each of you. I am profoundly grateful for the countless memories and moments we've shared together; these experiences truly embody the essence of life. Should I embark on a year-long cross-country journey, I'll make it a point to reach out to each one of you for a drink and a chat... once again.

Finally, thank you to every new individual from these last six years, too many to mention. If you seek the truth of who you are, journey until no one knows your name. A long stretch of road will teach you more about yourself than a hundred years of quiet introspection.

Abstract

Enhanced yield-mobility products in hybrid halide Ruddlesden–Popper compounds with aromatic ammonium spacers

by

Brian Barraza

This thesis explores the synthesis and characterization of novel hybrid halide Ruddlesden–Popper compounds, which are derivatives of three-dimensional AMX_3 perovskites, where A represents a monovalent cation, M a divalent metal cation, and X a halogen. The focus is on compounds with the general formula $(L)_2(CH_3NH_3)_{n-1}Pb_nI_{3_n+1}$, where L is a monovalent spacer cation, showcasing a layered crystal structure with perovskite-like layers separated by organic cation spacers. Two specific Ruddlesden–Popper compounds, incorporating a conjugated cation, 2-(4-biphenyl)ethylammonium (BPEA), were synthesized using solvothermal and solvent evaporation techniques.

The structural elucidation of these compounds, $(BPEA)_2PbI_4$ and $(BPEA)_2(CH_3NH_3)Pb_2I_7$, was achieved through X-ray crystallography. The ambient stability of these compounds was confirmed over time using powder X-ray diffraction. The investigation extended to the photoelectronic properties of these compounds, where transient photoconductance was measured by time-resolved microwave conductivity. Band-gap calculations of these two compounds was determined from

absorption spectra, resulting in optical properties comparable to those of simpler alkyl ammonium cation-based Ruddlesden–Popper compounds.

The comprehensive study presented herein not only advances the understanding of hybrid halide Ruddlesden–Popper compounds but also contributes to the development of materials with potential applications in optoelectronics, highlighting the synthesis methods, structural analysis, and functional characterization as essential tools in the material scientist's toolkit.

Contents

List of Figures

List of Tables

Chapter 1

Introduction

1.1 Motivation for advancements in optoelectronic materials

The global energy landscape is undergoing a significant transformation, driven by the escalating demand for energy and the imperative need to mitigate environmental impacts. In 2022, the world's energy consumption was quantified at 638 quadrillion British thermal units (Btu), continuing a trend of approximately 0.8% annual growth since 1970. Forecasts predict a 34% increase in energy consumption by 2050, underscoring the critical challenge of satisfying this demand sustainably.[1] In 2022, fossil fuels dominated primary energy production, accounting for 82% of the total energy

generated.[2] This dependency not only depletes natural resources but also exacerbates environmental degradation through the emission of greenhouse gases resulting from the combustion of fossil fuels. Carbon dioxide (CO_2) emissions, poised to rise by 15% in the next 25 years, contributed to 63.5% of the radiative forcing in 2022, a measure of climate change acceleration caused by greenhouse gases.[1, 3]

To put this into perspective we must look at the Annual Greenhouse Gas Index (AGGI). AGGI is calculated as the ratio of total direct radiative forcing due to greenhouse gases (noteworthy contributors are CO_2, CH_4, N_2O and chlorofluorocarbons) in a given year to its total in 1990. For 2022, the AGGI was 1.49, representing a 49% increase in total radiative forcing from anthropogenic emissions of these gases since 1990. Indeed, the surge in greenhouse gas concentrations since 1950 accounts for nearly three-fourths (71%) of the total AGGI increase over the last 270 years[4].

In the face of these daunting environmental challenges, the shift towards ”green” energy technologies emerges as a beacon of hope. The share of primary energy derived from non-fossil fuels is projected to expand anywhere from 29% and 34% by 2050, reflecting a global trend towards sustainable energy solutions.[1] Recent years have witnessed a marked increase in the economic viability of renewable energy sources, particularly solar and wind, which are now growing faster than any other energy sources. Progress in these fields is extremely important if we are to exnovate fossil fuels for environmentally friendly solutions to these issues. [5]

1.2 The rise of perovskite semiconductors as a viable alternative for green energy production

Amidst the current global energy landscape, the development of hybrid metal halides presents a promising avenue for optoelectronic applications in solar energy production. These materials, part of an emerging class of semiconductors, offer significant potential to further the advancement of green energy technologies.[6] Their advent and growing prominence in the field of solar energy highlights the broader movement towards environmentally friendly solutions that can address the dual challenges of meeting the world's increasing energy demands and mitigating the adverse effects of climate change.

1.2.1 A brief history of the perovskite

In charting the evolution of perovskite research, it's crucial to acknowledge the seminal contributions of pioneering scientists. The journey began with Gustav Rose's discovery of $CaTiO_3$ in Russia's Ural Mountains in 1839, which he named 'perovskite' after the mineralogist Lev Aleksevich von Perovski. Perovskites possess a distinct crystal structure composed of corner-connected octahedra, typically following the ABX_3 formula, where A and B are cations of different sizes, and X is an anion, resulting in

a highly connected, three-dimensional network (Fig1.1). This arrangement falls into various space groups, predominantly cubic, which contributes to their exceptional optical and electronic properties, rendering them ideal for a wide range of applications

.

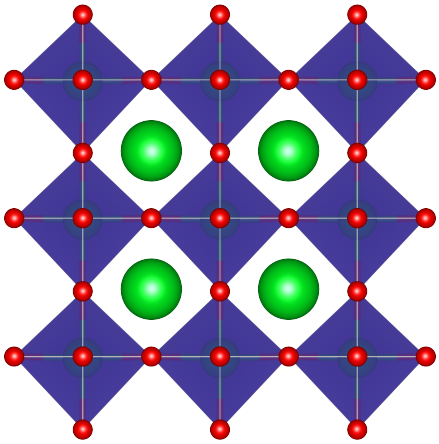

Figure 1.1: $BaTiO_3$ structure which illustrates the high dimensionality and connectivity of the the perovskite material class.[7]

Wells' introduction of synthetic techniques in 1893 provided the basis for advancing our comprehension of these compounds.[8]. Later, in 1926, Goldschmidt proposed that a solid will only assume the perovskite structure if the respective ionic radii R_A, R_B, and R_X fulfill the relation:

$$R_A + R_X = t \times \sqrt{2}(R_B + R_X)$$

With the tolerance factor, t, ranging between 0.8 and 1.[9] This criterion estab-

lished a mathematical foundation for predicting the formation of perovskite structures, quantitatively linking the ionic radii of constituent elements to the structural stability of perovskites through the tolerance factor, thus offering a pivotal tool for the design and discovery of new perovskite materials. Yet, it was Helen Dick Megaw's research on $BaTiO_3$, and later $NaNbO_3$, that effectively demonstrated how the structural and geometric characteristics of these materials influenced their properties, such as ferromagnetism, thus marking a significant leap in deciphering the true powers hidden inside the perovskite's highly tunable structure.[10–12] Further progress was marked by Weber's 1978 work on $CH_3NH_3PbI_3$, a variation of the perovskite structure where the alkyl ammonium CH_3NH_3 is used for the A cation.[13] $CH_3NH_3PbI_3$ garnered significant attention as its application in solar cells started to evolve. Initially, research on perovskites was limited to their geological and material aspects, concentrating on their distinct crystallography, magnetic, and conductive properties. Such foundational exploration set the stage for realizing their wider capabilities.

1.2.2 Meteoric rise in efficiencies

The ascent of hybrid halide semiconductors in green energy has been marked by pivotal developments, transforming them into a cornerstone of sustainable technology. The journey began with notable breakthroughs between 2009 and 2012, where the foundational work by Miyasaka and co-workers introduced liquid-based dye-sensitized solar cells employing nanocrystals of $MAPbI_3$ on a TiO_2 surface.[14] However, the

field witnessed a paradigm shift in 2012 with several key developments: Kanatzidis and co-workers unveiled all-solid-state dye-sensitized cells using $CsSnI_3$ perovskite as both a hole transport layer and light absorber, achieving around 10% efficiency;[15] Miyasaka, Snaith, and their teams developed a solid-state cell in which structured films of titania or alumina nanoparticles were solution coated with $MAPbI_3$;[16] and Park and colleagues independently confirmed the solid layer perovskite of $MAPbI_3$ in these systems.[17] These milestones significantly accelerated advancements in perovskite solar cell (PSC) technology, which, as of this writing, have propelled efficiencies beyond 26%, a figure that rivals established inorganic semiconductors.[18, 19]

Despite these achievements, concerns with the efficacy of these materials arose, particularly regarding the long-term stability of devices and the toxicity of lead. Three-dimensional hybrid perovskites using $CH_3NH_3PbI_3$ have been shown to be susceptible to degradation (the materials will rapidly degrade into the precursor reagents, lead iodide and the respective alkylammonium iodide) from heat, light, and moisture, hampering their long-term device stability.[20–25] Addressing these challenges became paramount to advancing the technology further.

1.2.3 Advantages of the layered 2D phase

2D perovskites, represented by the formula $(A')_m(A)_{n-1}B_nX_{3n+1}$, introduce a novel structural and compositional element, A'. Here, A' can be either a monovalent cation ($m = 2$, Ruddlesden-Popper, RP phase) or a divalent cation ($m = 1$, Dion-Jacobson,

DJ phase), which intercalates between the anion layers, "breaking-up" the anionic B-X octahedral network resulting in 2D perovskite sheets. This new feature introduces structural complexity and enables property customization, partly through a variety of new phase transitions.[26]

2D perovskites have attracted attention for their superior environmental durability relative to their three-dimensional counterparts. The enhanced stability of R–P perovskites has been attributed to the increased hydrophobicity from the organic layer from by the A' cations.[20–25] The addition of this organic layer, however, leads to highly anisotropic charge transport resulting in higher rates of charge carrier recombination, a consequence of the reduced dimensionality in the metal-iodide networks due to quantum confinement effects.[27]

In essence, the increased stability of the 2D phases comes at the cost of the higher efficiencies of the 3D phase. However, progress in this domain may come from combining the two phases in order to address the issues with stability in the 3D phase and circumvent the physical limitations of the 2D phase. 2D/3D perovskite heterostructure with an impressive efficiency of 19.4% were created by applying n-butylammonium bromide via spin coating resulting in the formation of a slender RP perovskite layer of intermediate phases. This method effectively used the best of both worlds by inserting a 2D RP structure between the 3D $CH_3NH_3PbI_3$ perovskite and the hole transport layer (HTL) of the device, thus reducing nonradiative recombination within the perovskite absorber layer while simultaneously adding enhanced environmental stability.[28] To

lay the groundwork for future studies in the domain of perovskite solar cells (PSCs), highlighting the use of 2D perovskite as a ”buffer” for the HTL is essential.

1.3 Future outlook of hybrid perovskites in solar technology

In 2022, the solar power sector celebrated a historic milestone by surpassing the 1 TW benchmark for solar capacity.[29] To put this into perspective, the average U.S. household consumes about 10,649 kilowatt-hours (kWh) of electricity per year. 1 TW (or 1,000,000,000 kW) operating for just one hour (1 TWh) would be enough to power nearly 94 million average U.S. homes for that hour. Given that the sun doesn't shine all the time, PV systems have a capacity factor (the ratio of actual output over a period of time to the potential output if it had operated at full capacity the entire time) that varies by location but can be roughly estimated at 20-25% on average. Even at a 20% capacity factor, 1 TW of PV capacity could still generate significantly more electricity annually than many countries consume.[2, 30, 31] The share of global electricity produced by photovoltaics increased from 3.6% in 2021 to 4.5% in 2022, reflecting a significant 25% growth in the proportion of electricity generated from solar compared to all sources, a trend that is only expected to continue to grow.[1]

The economic feasibility of PSCs presents a promising outlook, especially when juxtaposed with the cost metrics of more established PV technologies, such as III-V

semiconductors. According to a technoeconomic assessment reported by the National Renewable Energy Laboratory, III-V technologies, while advanced, have been confined to niche applications due to their high manufacturing selling price (MSP) of $77/W. Even with projected cost reductions, these remain at a projected $20/W, significantly higher than other technologies.[19]

In stark contrast, the MSP for single-junction sheet-to-sheet perovskite modules is estimated at a mere $0.38/W at small production scales. With anticipated advancements and economies of scale, this cost could potentially decrease to $0.18/W, underscoring the cost-effective nature of perovskite technology. Furthermore, the MSP for perovskite-on-silicon (Si) tandem modules stands at $0.31/W in early production, based on pilot production outcomes. This indicates not only the affordability of perovskite PV technologies but also their potential for further cost reductions as the technology matures and scales up.[19, 32, 33]

The disparity in cost between perovskite PVs and established III-V semiconductors highlights the substantial economic advantage of adopting perovskite technology for broader applications. The affordability of perovskites positions PSCs as a transformative solution in the quest for affordable, efficient, and scalable renewable energy sources. This economic feasibility, combined with ongoing technological advancements, makes PSCs an increasingly viable option for mainstream solar energy applications, promising to play a pivotal role in the future of renewable energy.

In summary, the rise of hybrid halide semiconductors as a viable form of green

energy encapsulates a journey of innovation, from early experimental setups to achieving record-breaking efficiencies and addressing scalability for commercial applications. Despite hurdles such as stability and lead toxicity, the relentless pursuit of solutions continues to drive the field towards a sustainable future, making PSCs a beacon of green energy potential.

Chapter 2

Enhanced yield-mobility products in hybrid halide Ruddlesden–Popper compounds with aromatic ammonium spacers

Hybrid halide Ruddlesden–Popper compounds are related to three-dimensional hybrid AMX_3 perovskites (e.g. where A is a monovalent cation, M is a divalent metal cation, and X is a halogen) with the general formula $L_2A_{n-1}M_nX_{3_n+1}$where L is a monovalent spacer cation. The crystal structure comprises perovskite-like layers separated by

[1]Naveen R. Venkatesan, Ali Mahdi, Guang Wu, Michael L. Chabinyc, and Ram Seshadri have contributed to the contents of this chapter.

organic cation spacers. In this chapter two Ruddlesden–Popper compounds with a conjugated cation, 2-(4-biphenyl)ethylammonium (BPEA) prepared by solvothermal and solvent evaporation techniques are discussed. The structures of the two compounds: $(BPEA)_2PbI_4$ and $(BPEA)_2(CH_3NH_3)Pb_2I_7$, were solved by X-ray crystallography. The aromatic rings of the BPEA groups are well-separated in the organic layers leading to optical properties comparable to $n = 1$ and 2 hybrid halide Ruddlesden–Popper compounds with simpler alkyl ammonium cations. The ambient stability of both compounds over time was also confirmed by powder X-ray diffraction. Finally, the transient photoconductance, measured by timeresolved microwave conductivity, show that the compounds have maximum yield-mobility products respectively of $0.07\,cm^2\,V^{-1}\,s^{-1}$ and $1.11\,cm^2\,V^{-1}\,s^{-1}$ for $(BPEA)_2PbI_4$ and $(BPEA)_2(CH_3NH_3)Pb_2I_7$, both slightly enhanced over what has been measured for compounds with n-butylammonium spacer cations.

Previous publication of this data can be found in *Dalton Transactions*, © 2019 The Royal Society of Chemistry, reprinted with permission.

Venkatesan, N. R.; Mahdi, A.; Barraza, B.; Wu, G.; Chabinyc, M. L.; Seshadri, R. Enhanced yield-mobility products in hybrid halide Ruddlesden–Popper compounds with aromatic ammonium spacers, *Dalton Trans*. **2019**, 48, 14019–14026.

[1]Naveen R. Venkatesan, Ali Mahdi, Guang Wu, Michael L. Chabinyc, and Ram Seshadri have contributed to the contents of this chapter.

2.1 Introduction

Hybrid organic–inorganic perovskites (HOIPs) are solutionprocessable semiconductors with a diversity of structures allowed by the combination of organic and inorganic groups.[34–40] The power conversion efficiency (PCE) of photovoltaic devices composed of hybrid perovskite alloys (based on $CH_3NH_3PbI_3$ and $HC(NH_2)_2PbI_3$) has increased to 26.1% very quickly,[18, 41, 42] competitive with other thin film technologies such as CIGS[43] and CdTe.[42] Additionally, HOIPs have shown great synthetic tunability, allowing control of emission energies, making them promising for light emission applications.[44–53] However, three-dimensional hybrid perovskites have been shown to be susceptible to degradation from heat, light, and moisture, hampering their long-term device stability.[20–25]

The class of two-dimensional layered perovskite compounds known as Ruddlesde–Popper (R–P) compounds, have been synthesized using organic ammonium and main group cations and halide anions. These compounds usually display enhanced stability in ambient conditions.[54–57] The R–P compounds have a general stochiometric formula of $(L)_2(CH_3NH_3)_{n-1}Pb_nI_{3_n+1}$, where L represents a large organic cation that serves to break up the three-dimensional connectivity of the perovskite crystal structure and n represents the number of lead iodide octahedra in the inorganic layer.[58, 59] The enhanced stability of R–P perovskites has been attributed to the

increased hydrophobicity from the organic layer from by the L cations.[60–62] The addition of this organic layer, however, leads to highly anisotropic charge transport, and devices based on two-dimensional perovskites have only achieved PCE values close to 15%.[55, 63] The wider band gaps of two-dimensional perovskites relative to three-dimensional perovskites does provide the benefit of tuning the emission in light emitting diodes.[47, 48, 50] Recent efforts to embed two-dimensional perovskite moieties into the overall three-dimensional perovskite matrix have also yielded efficiencies closer to that of champion devices, with some increased stability.[64–66] The majority of studies have focused on alkylammonium L cations, and these compounds have resulted in the highest photovoltaic efficiencies to date for two-dimensional perovskite compounds.[55, 60, 67–69] Various conjugated ions have also been incorporated into the Ruddlesder–Popper structure, [45, 70, 71] including thiophenes,[72, 73] and the single phenyl analog of the structures reported here, phenethylammonium.[54, 74] Finally, recent efforts have embraced other layered perovskite motifs such as Dion–Jacobson compounds.[75, 76] Controlling the properties of lower dimensional perovskites by varying the L cation is desirable for tuning the electronic properties of the materials system either in pure systems or in composites.

We report here two Ruddlesden–Popper compounds using the aromatic organic cation 2-(4-biphenyl)ethylammonium (BPEA), resulting in the compounds $(BPEA)_2PbI_4$ ($n = 1$) and $(BPEA)_2(CH_3NH_3)Pb_2I_7$ ($n = 2$). These compounds were synthesized by solvothermal and solvent evaporation techniques, and the resulting

crystal structures were solved from X-ray crystallography. Structural measurements after aging in ambient conditions show that both compounds are stable without encapsulation. The optical absorbance was measured with ultraviolet-visible spectroscopy, and the charge transport was characterized by time-resolved microwave conductivity (TRMC). By utilizing TRMC, carrier dynamics in the synthesized powders could directly be measured without device formation.

2.2 Experimental details

Single crystals of $(BPEA)_2PbI_4$ were prepared through solvothermal methods. A stoichiometric ratio of lead(II) iodide (PbI_2, 160.0 mg), 2-(4-biphenyl)ethylamine (BPEA, 68.0 mg), and aqueous (57 wt% in H_2O) hydroiodic acid (HI, 2 mL) were added to a pressure vessel (23 mL PTFE-lined stainless steel Parr autoclave). The temperature of the reaction vessel was ramped to 150 °C over 2 hours, held for 8 hours, and then allowed to cool to room temperature over 7.5 hours. Resulting bright-orange crystals were then washed with diethyl ether ($(C_2H_5)_2O$) and dried under vacuum for one day. Solvothermal synthesis of $(BPEA)_2PbI_4$ was required to produce single-crystals of sufficient size for X-ray crystallography.

Bulk crystals of $(BPEA)_2(CH_3NH_3)Pb_2I_7$ were prepared via solvent evaporation – a stoichiometric ratio of previously synthesized $(BPEA)_2PbI_4$(30 mg), PbI_2 (24.9 mg), and methylammonium iodide (CH_3NH_3I, 8.6 mg) were dissolved in a $2:1$ mixture

(volume/volume) of acetone and nitromethane (15 mL). The mixture was stirred and heated at 90 °C to form a pale-yellow solution. The solvent was transferred to a vial and allowed to evaporate at room temperature for one day. Resulting crystals were washed with diethyl ether and dried under vacuum for one day. For single-crystals of sufficient size and quality for X-ray crystallography a stoichiometric ratio of previously synthesized $(BPEA)_2PbI_4$(30 mg), PbI_2 (24.9 mg), and methylammonium iodide (CH_3NH_3I, 8.6 mg) were dissolved in a 2 : 1 mixture (volume/volume) of acetone and nitromethane (15 mL) along with 12.1mg of NaI (3 : 1 molar ratio with $(BPEA)_2PbI_4$) The mixture was stirred and heated at 90 °C to form a pale-yellow solution. The solvent was transferred to a vial and allowed to evaporate at room temperature. After one day a sample of this solution was transferred to a glass slide and allowed to evaporate for 5 additional days, yielding bright-red crystals. Unable to grow single crystals of $n \geq 3$ despite using precisely controlled synthetic methods.[77]

Single Crystal X-ray diffraction data for $(BPEA)_2PbI_4$ and $(BPEA)_2(CH_3NH_3)Pb_2I_7$ was collected on a Bruker KAPPA APEX II diffractometer equipped with an APEX II CCD detector using a TRIUMPH monochromator with a Mo Kα X-ray source (λ= 0.71073Å). The crystals were mounted on a cactus needle with Paratone-N oil and kept under nitrogen. Absorption correction of the data was carried out utilizing the multi-scan method SADABS.[78] Further calculations were done using SHELXTL.[79] The low bond precision in carbon bonds is due to the disorder and poor contrast near to heavier elements. All hydrogen atom positions were omitted. Structures were determined

using direct methods,[80] and he graphical depictions used in the main paper were done with the program VESTA.[81]

Product purity was established via Powder X-ray diffraction (PXRD) aquired using a Panalytical Empyrean powder diffractometer in reflection mode with a Cu-Kα source, operating with an accelerating voltage of 45 kV and a beam current of 40 mA. Simulated diffraction patterns were calculated using the General Structure Analysis System (GSAS).[82, 83] For simulated diffraction patterns containing preferred orientation, March–Dollase orientational correction factors were used.[84]

Absorption spectra were determined by grinding crystals into powders and measuring diffuse reflectance with a Shimadzu UV-2600 ultraviolet-visible spectrophotometer equipped with an integrating sphere. The compounds tested were suspended in BaSO4 medium (via grinding). Reflectance data were converted to absorbance using the Kubelka–Munk equations.[85]

TRMC measurements were conducted with an experimental setup described previously.[86–88] A Sivers IMA VO4280X/00 voltage-controlled oscillator (VCO) (approximate power of 16 dBm and a tunable frequency range of 8–15 GHz) was used to generate a microwave frequency signal. The signal was then directed into a Fairview Microwave SFC0712 electronic circulator, a three-port device that rotates signals from port 1 to port 2 and signals from port 2 to port 3. The signal from port 2 was then fed into a Fairview Microwave 90AC206 SMA to X-band waveguide and is coupled to an X-band cavity with homebuilt coupling iris and tuning screw. The cavity operates in

TE_103 mode, and a homemade copper plate with slots along the direction of microwave current allows optical access to the sample. The microwaves form standing waves and the tuning screw allows for over coupling, critical coupling, and under coupling to the cavity – all experiments reported were performed in the under coupled regime. The powder samples were mounted to the inside of the cavity with double-sided tape and placed at the maximum of the microwave electric field. Reflected microwaves are directed to a Fairview Microwave SMD0218 zero-bias Schottky diode detector, operating in the linear regime. The rectified signal was amplified by a three stage, DC-coupled wide-band amplifier consisting of Texas Instruments THS3091 operational amplifiers. For the reference signal, the microwave signal was split at the source to normalize the reflected power from the cavity. The amplified signal and reference were detected using a Textronix TDS 3032C digital oscilloscope. Free carriers are generated in the powder samples through illumination with a Continuum Minilite pulsed Nd:YAG 532 nm laser (FWHM of $\sim$5 ns), which drift under the influence of the microwave signal with a velocity proportional to their mobility $v = \mu E$. The change in reflected microwave intensity is then used to determine the transient photoconductance which, in turn, is used to calculate the TRMC figure-of-merit: $\phi \sum \mu$ (yield-mobility product) at each fluence.[89]

2.3 Results and discussion

The structures of $(BPEA)_2PbI_4$ and $(BPEA)_2(CH_3NH_3)Pb_2I_7$, solved from single-crystal X-ray diffraction at 100 K, are shown in Figure 2.1, visualized along the [010] crystallographic direction for $(BPEA)_2PbI_4$ and [001] for $(CH_3NH_3)Pb_2I_7$ using VESTA.[81] The parameters of the structure solutions of each compound are shown in Table 2.1, and single-crystal diffraction images are shown below in Figures 2.2 and 2.3.

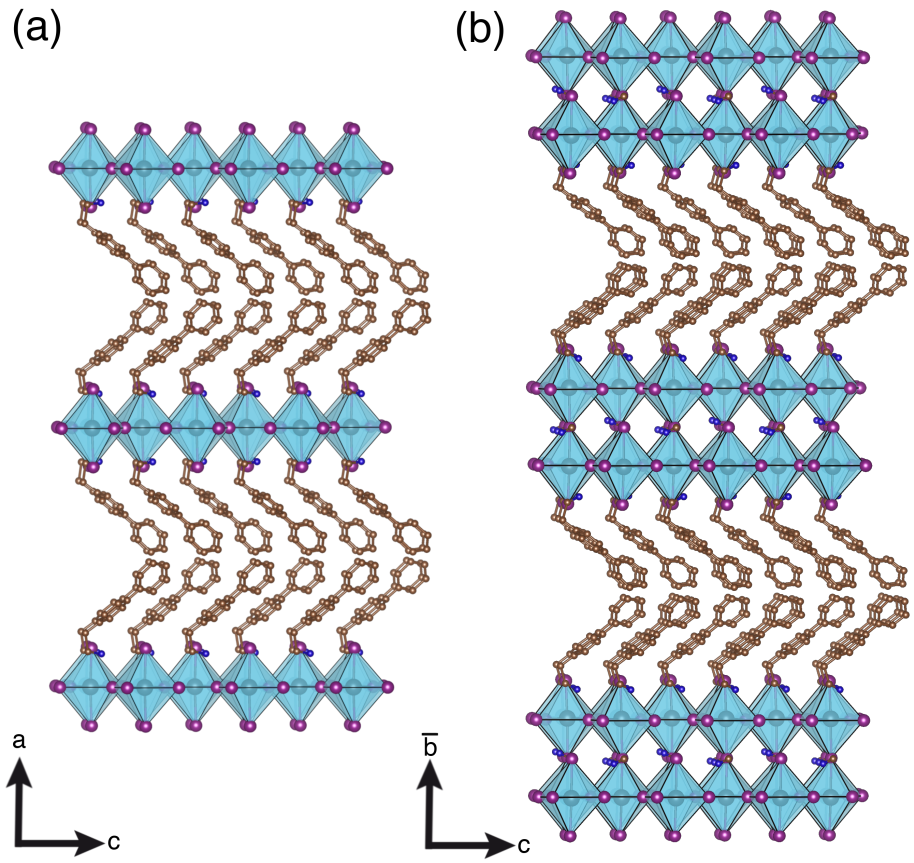

Figure 2.1: (a) Crystal structures of $(BPEA)_2PbI_4$ and (b) $(BPEA)_2(CH_3NH_3)Pb_2I_7$ solved by single-crystal X-ray diffraction, projected down the b and a crystallographic axes, respectively. The BPEA cations pack diagonally, are eclipsed with each other, and do not interdigitate.

Table 2.1: Crystallographic information for $(BPEA)_2PbI_4$ and $(BPEA)_2(CH_3NH_3)Pb_2I_7$, 100 K

Empirical formula	$(BPEA)_2PbI_4$	$(BPEA)_2(CH_3NH_3)Pb_2I_7$
Crystal habit and color	Plate, orange	Plate, red
Crystal system	Orthorhombic	Orthorhombic
Space group (#)	*Cmc*2_1 (36)	*Aba*2 (41)
Volume (Å^3)	3250.8(8)	4199.5(6)
Temperature (K)	100(2)	100(2)
a (Å)	42.920(6)	8.7633(8)
b (Å)	8.7431(11)	55.030(5)
c (Å)	8.6629(14)	8.7081(7)
α (°)	90	90
β (°)	90	90
γ (°)	90	90
Z	4	4
ρ (g mol^{-1})	1107.32	1731.30
Dens. (g cm^{-3})	2.263	2.738
Abs. (mm^{-1})	9.007	13.176
F_{000}	2016	3072
Reflections	10 433 (2500)	9269 (3551)
R_{int}	0.0927	0.0861
R_1	0.0533	0.0653
wR_2	0.0892	0.1471
∂F (e Å^{-3})	2.612 & -1.446	4.473 & -5.449
GOF	1.436	1.095

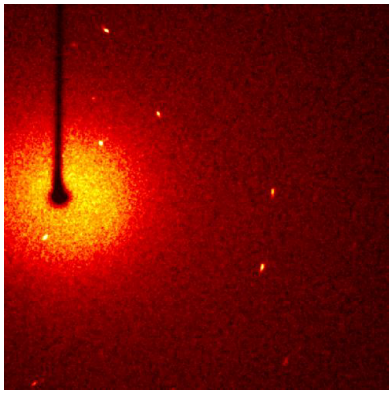

Figure 2.2: Sample X-ray diffraction image of $(BPEA)_2PbI_4$ obtained from grown single-crystals.

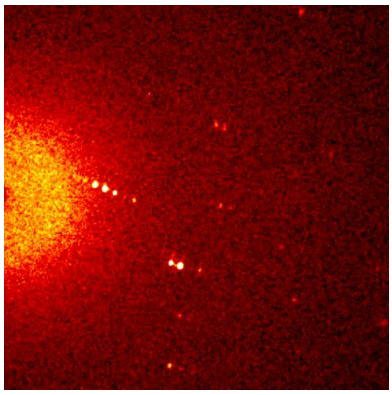

Figure 2.3: Sample X-ray diffraction image of $(BPEA)_2(CH_3NH_3)Pb_2I_7$ obtained from grown single-crystals.

Both compounds have orthorhombic unit cells and the diffraction data were fit best by non-centrosymmetric space groups. The organic BPEA moieties form symmetric bilayers in both compounds, while the inorganic framework in the two perovskites consists of corner-sharing lead iodide octahedra. The organic bilayer formed between the lead iodide sheets is consistent with previously reported hybrid halide Ruddlesden–Popper structures with other organic cation spacers.[55, 72, 74, 90] The BPEA moieties from subsequent layers do not interdigitate, preventing π-π interactions between L groups on each lead iodide layer. If we consider that the n-butylammonium cation would fit into a cylinder with a diameter of $\sim$1.5 Å and it forms a bilayer structure rather than interdigitating, it is unsurprising that 2-(4-biphenyl)ethylammonium which packs with a closest C–C distance between phenyl rings of $\sim$3.4 Å, also forms separate layers. The widest region of the phenyl ring has a diameter of $\sim$4 Å, so this aromatic packing distance is required when accounting for bond rotations. The separation distance between the lead iodide layers is $\sim$15 Å in $(BPEA)_2PbI_4$ and $(BPEA)_2(CH_3NH_3)Pb_2I_7$, compared to $\sim$10 Å in $(PEA)_2PbI_4$ and $(PEA)_2(CH_3NH_3)Pb_2I_7$.[71, 90] There is a slight difference in the layer spacing between the BPEA $n = 1$ (15.0 Å) and $n = 2$ (14.7 Å) that may be due to slightly more efficient packing in the $n = 2$ compound; regardless, the organic layers appear to be consistent in size.

Table 2.2: Select bond distances and angles of $(BPEA)_2PbI_4$ and $(BPEA)_2(CH_3NH_3)Pb_2I_7$

	$(BPEA)_2PbI_4$	$(BPEA)_2(CH_3NH_3)Pb_2I_7$
	Bond Distances	
Pb-I$_{\text{axial (1)}}$ (Å)	3.2073(14)	3.131(3)
Pb-I$_{\text{axial (2)}}$ (Å)	3.2073(14)	3.2617(12)
Pb-I$_{\text{axial (3)}}$ (Å)	N/A	3.2617(12)
Pb-I$_{\text{axial (4)}}$ (Å)	N/A	3.131(3)
Pb-I$_{\text{equatorial (1)}}$ (Å)	3.108(5)	3.141(4)
Pb-I$_{\text{equatorial (2)}}$ (Å)	3.174(5)	3.179(3)
Pb-I$_{\text{equatorial (3)}}$ (Å)	3.222(5)	3.191(4)
Pb-I$_{\text{equatorial (4)}}$ (Å)	3.154(5)	3.157(4
	Bond Angles	
I-Pb-I$_{\text{axial (1)}}$(°)	176.4(3)	176.38(9)
I-Pb-I$_{\text{axial (2)}}$(°)	N/A	176.38(9)
I-Pb-I$_{\text{equatorial (1)}}$(°)	179.25(14)	176.31(8)
I-Pb-I$_{\text{equatorial (2)}}$(°)	178.18(16)	176.28(9)
Pb-I-Pb$_{\text{axial}}$(°)	N/A	179.2(3)
Pb-I-Pb$_{\text{equatorial}}$(°)	152.49(15)	154.52(11)

Table 2.3: Select bond distances and angles of $(BA)_2PbI_4$ and $(BA)_2(CH_3NH_3)Pb_2I_7$

	$(BA)_2PbI_4$	$(BA)_2(CH_3NH_3)Pb_2I_7$
	Bond Distances	
Pb-I$_{\text{axial (1)}}$ (Å)	3.201(16)	3.08(3)
Pb-I$_{\text{axial (2)}}$ (Å)	3.213(13)	3.28(3)
Pb-I$_{\text{axial (3)}}$ (Å)	N/A	3.25(3)
Pb-I$_{\text{axial (4)}}$ (Å)	N/A	3.08(3)
Pb-I$_{\text{equatorial (1)}}$ (Å)	3.164(7)	3.171(4)
Pb-I$_{\text{equatorial (2)}}$ (Å)	3.212(8)	3.169(5)
Pb-I$_{\text{equatorial (3)}}$ (Å)	3.191(6)	3.169(5)
Pb-I$_{\text{equatorial (4)}}$ (Å)	3.160(7)	3.171(4)
	Bond Angles	
I-Pb-I$_{\text{axial (1)}}$(°)	178.6(3)	177.3(3)
I-Pb-I$_{\text{axial (2)}}$(°)	N/A	177.3(3)
I-Pb-I$_{\text{equatorial (1)}}$(°)	179.2(5)	175.5(9)
I-Pb-I$_{\text{equatorial (2)}}$(°)	179.1(5)	175.5(9)
Pb-I-Pb$_{\text{axial}}$(°)	N/A	165.64(16)
Pb-I-Pb$_{\text{equatorial}}$(°)	155.1(3)	164.2(10)

Geometric details of both crystal structures, including bond lengths for the four equatorial and two axial iodides along with all I–Pb–I and Pb–I–Pb (if applicable) bond angles are tabulated in Table 2.2. For comparison, the bond lengths and angles from $(BA)_2PbI_4$ and $(BA)_2(MA)Pb_2I_7$ are listed in Table 2.3.[72, 91] The octahedra in the lead iodide layers in both $(BPEA)_2PbI_4$ and $(BPEA)_2(CH_3NH_3)Pb_2I_7$ are highly tilted in plane, with equatorial Pb–I–Pb bond angles of approximately 155 ° in both structures. The measured bond lengths in both compounds are consistent (i.e. independent of L cation used) with previous observations in other hybrid halide Ruddlesden–Popper compounds, however the out of plane tilt between connected Pb–I octahedra (in the $n = 2$) are much stiffer (179.2 °) compared to $(BA)_2(MA)Pb_2I_7$.

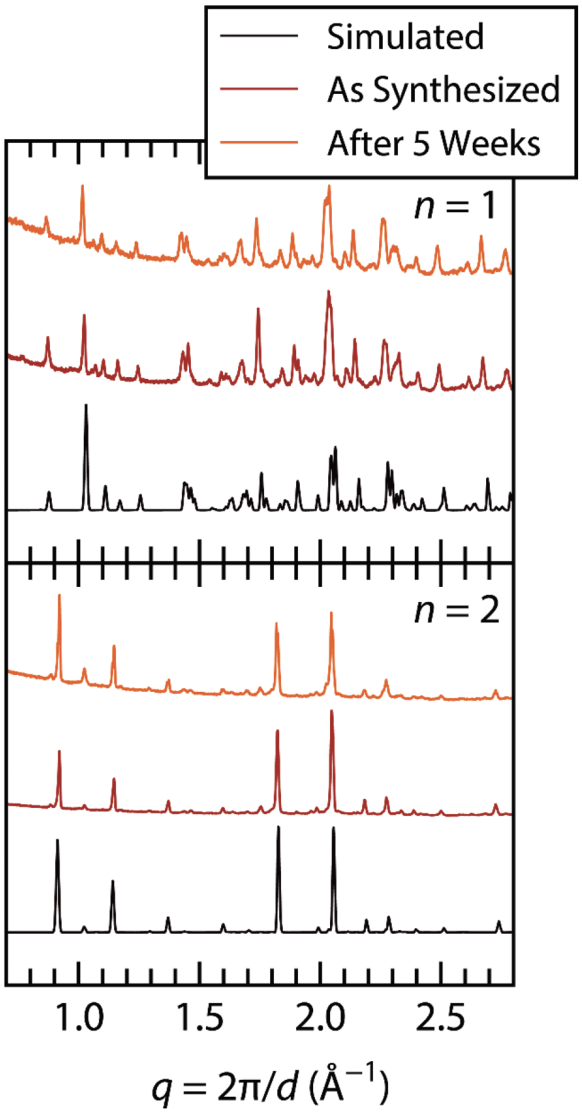

Figure 2.4: Powder X-ray diffraction (PXRD) patterns of $(BA)_2PbI_4$ ($n = 1$) and $(BPEA)_2(CH_3NH_3)Pb_2I_7$ ($n = 2$) both after preparation and after five weeks of aging in ambient conditions, along with simulated PXRD patterns of solved structures shown in Fig. 2.1

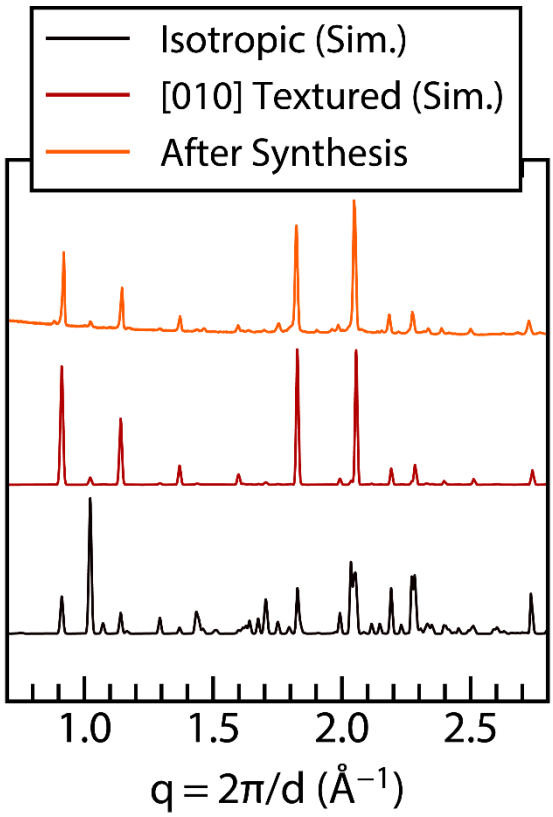

Figure 2.5: Powder X-ray diffraction of synthesized powder of $(BPEA)_2(CH_3NH_3)Pb_2I_7$ compared to simulated diffraction patterns of an isotropic sample and a [010]-textured sample, illustrating structural agreement with the latter.

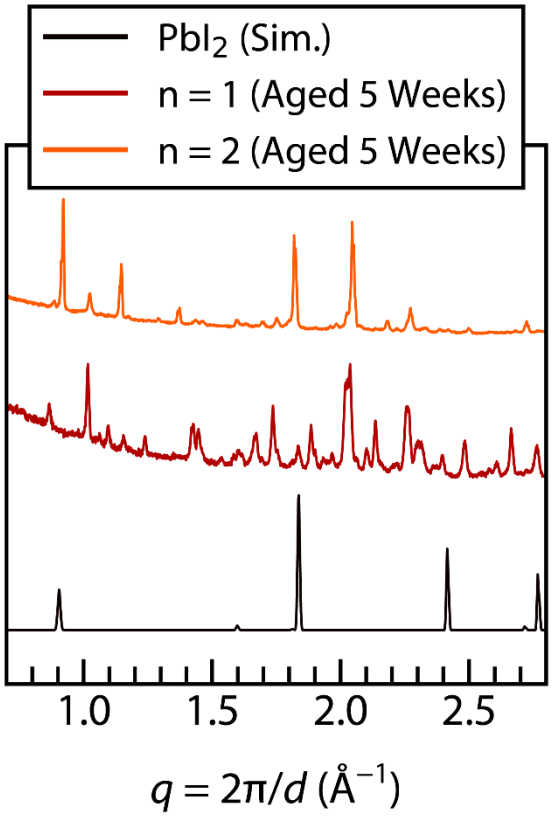

Figure 2.6: Powder X-ray diffraction patterns of $(BPEA)_2PbI_4$ and $(BPEA)_2(CH_3NH_3)Pb_2I_7$ powders aged for five weeks in ambient conditions, along with simulated diffraction pattern of PbI_2. Comparison with the simulated pattern illustrates no degradation of Ruddlesden–Popper phases into lead iodide.

Because bulk characterization measurements were carried on powders consisting of crushed single-crystals, solved crystal structures were used to simulate powder X-ray diffraction (PXRD) patterns for comparison. Simulated diffraction patterns were generated as described in the Experimental section. Fig. 2.4 shows PXRD measurements of crushed crystals of $(BPEA)_2PbI_4$ and $(BPEA)_2(CH_3NH_3)Pb_2I_7$ both immediately after preparation and after five weeks of aging in ambient conditions, along with their simulated diffraction patterns. To capture the correct structural behavior in $(BPEA)_2(CH_3NH_3)Pb_2I_7$, the simulated diffraction pattern included texturing along the [010] crystallographic direction, which is the lead iodide layer stacking direction (Fig. 2.1). It is possible that due to the tendency of these $n = 2$ crystals to grow as anisotropic flakes, the resulting powder retains some crystalline texture. If the slow growth direction during preparation was along this stacking direction (due to the incorporation of the BPEA layer), it is consistent with the flake-like crystals. This is evident when compared to a simulation of an isotropic sample of $(BPEA)_2(CH_3NH_3)Pb_2I_7$, in which the relative peak height intensities do not match well with our measurement (Fig. 2.5). In both the $n = 1$ and $n = 2$ compounds, the position and intensities of peaks in the diffraction patterns show no change after five weeks of aging. This suggests that $(BPEA)_2(CH_3NH_3)_{n-1}Pb_nI_{3n+1}$ possesses increased stability relative to three-dimensionally connected perovskites, a property that has been widely observed in layered perovskite compounds.[54, 55, 92] The subtle differences in relative peak heights between the as-synthesized and aged samples is likely due to the slight variations in

the overall crystalline texturing from the loading of the powder samples for measurement. Ultimately, the structural measurements on both compounds show no formation of PbI_2 (Fig. 2.6) and no other degradation upon aging in ambient conditions.

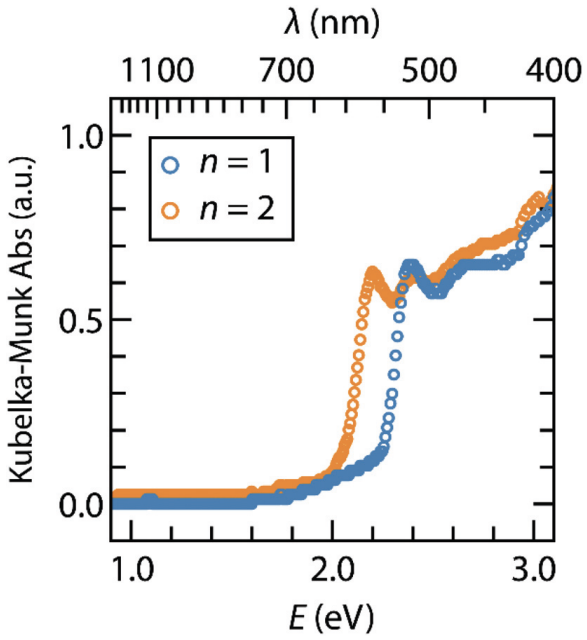

Figure 2.7: Optical absorbance of $(BPEA)_2PbI_4$ ($n = 1$) and $(CH_3NH_3)Pb_2I_7$ ($n = 2$) measured from diffuse reflectance of powder samples. Reflectance data were converted into absorbance values using the Kubelka–Munk equations and show excitonic features at 2.4 eV and 2.2 eV for $n = 1$ and 2, respectively.

The optical absorbances of both layered perovskite compounds were measured and are presented in Fig. 2.7, showing expected behavior. Due to the large optical density of both powder samples, absorbances were measured by taking diffuse reflectance data and transforming them according to the Kubelka–Munk equations.[85] In both cases, clear excitonic features are visible at the optical absorbance onset, con-

sistent with the quantum confined structure of the Ruddlesden–Popper compounds. In $(BPEA)_2PbI_4$, the peak attributed to excitonic absorption occurs at 2.4 eV, while in $(BPEA)_2(CH_3NH_3)Pb_2I_7$, it appears at 2.2 eV. Both of these energies are equal to previously measured exciton energies in Ruddlesden–Popper systems containing both butylammonium and phenethylammonium spacer groups.[74, 86]

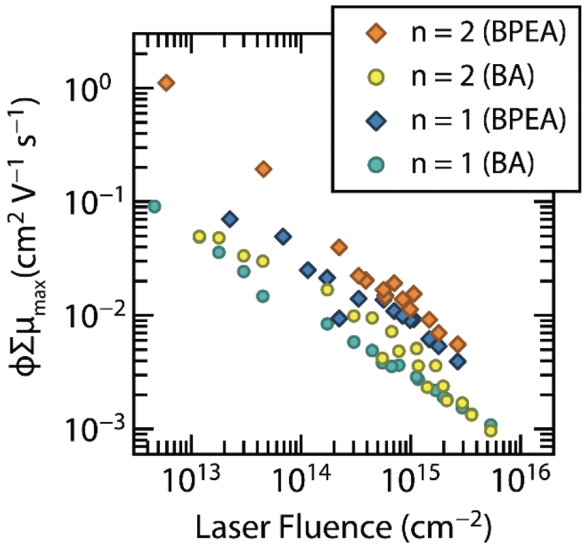

Figure 2.8: Maximum value of the TRMC figure-of-merit $\phi \sum \mu$ over a wide range of excitation laser fluences for $(BPEA)_2PbI_4$ ($n = 1$) and $(BPEA)_2(CH_3NH_3)Pb_2I_7$ ($n = 2$), along with TRMC data of $(BA)_2PbI_4$ ($n = 1$) and $(BA)_2(CH_3NH_3)Pb_2I_7$ ($n = 2$).[86] Monotonic increases seen with decreasing fluence are characteristic of shorter carrier lifetimes and larger recombination rate coefficients compared to $MAPbI_3$.

The charge carrier dynamics of these two compounds were analyzed using time-resolved microwave conductivity (TRMC).[86, 87, 93–99] Excitation of the compounds with a pulse of light with energy above the band gap creates free carriers and excitons. Only the free carriers then interact with the microwave electric field (frequency range of 8–9 GHz) and the attenuation of this applied microwave signal, caused by carrier drift, can be then used to calculate the transient photoconductance in the sample. Using these photoconductance measurements, a value for the TRMC figure-of-merit can be determined:

$$\phi \sum \mu$$

The figure-of-merit is the product of ϕ (the yield of free carriers per incident photon) and the sum of the electron and hole mobilities:

$$\sum \mu = \mu_e + \mu_h$$

The value of $\phi \sum \mu$ at short times after the excitation pulse typically exhibit strong laser fluence dependence due to recombination of electron hole pairs.[93, 100] Fluence-dependent measurements of $\phi \sum \mu$ were therefore collected for both $(BPEA)_2PbI_4$ and $(BPEA)_2(CH_3NH_3)Pb_2I_7$ and are shown in Fig. 2.8, along with previously measured values for $(BA)_2PbI_4$ and $(BA)_2(CH_3NH_3)Pb_2I_7$.[86] The lowest measurable fluence for both compounds was set by the signal-to-noise of our instrument for a given sample

amount and its figure-of-merit. Additionally, due the small size of the $(BPEA)_2PbI_4$ and $(BPEA)_2(CH_3NH_3)Pb_2I_7$ crystals, powders were measured rather than individual single-crystals in order to improve the signal-to-noise of the experiment. The peak yield-mobility products, $\phi \sum \mu_{max}$, for the $n = 1$ and 2 compounds are 0.07 $cm^2\,V^{-1}\,s^{-1}$ (at 2.25×10^{13} photons per cm^2) and 1.11 $cm^2\,V^{-1}\,s^{-1}$ (at 5.93×10^{12} photons per cm^2), respectively.

To understand the dependence of the TRMC data on incident fluence, we must consider the different charge recombination pathways in both compounds. Charge recombination in semiconductors is governed by the rate equation:

$$R = k_1 n(t) + k_2 n(t)^2 + k_3 n(t)^3$$

where $n(t)$ is the instantaneous carrier concentration and k_1, k_2, and k_3 are the rate constants of monomolecular, bimolecular, and trimolecular or Auger recombination, respectively.[86–88, 100] By changing the incident laser fluence, we can change the initial carrier concentration and observe the effects of recombination at short times, i.e. if there is significant recombination during the excitation pulse width (∼5 ns) and response time of the cavity (∼60 ns). Therefore, at low initial carrier concentrations, it is expected that the recombination dynamics are dominated by monomolecular recombination – since the recombination rate is linear with $n(t)$ in this regime, we would expect the TRMC plot to have a very shallow slope on a logarithmic scale because little

recombination occurs at short times. Such behavior is observed in TRMC of methylammonium lead iodide at low laser fluences.[86, 87, 93] As the laser fluence and carrier concentration increases, both bimolecular and Auger recombination pathways become more active and the dependence of $\phi \sum \mu$ becomes increasingly more negative. We see an overall monotonic increase in $\phi \sum \mu$ for both compounds with decreasing laser fluence and do not see a plateau characteristic of monomolecular recombination. This dependence has been observed in previous TRMC measurements of layered hybrid halides and has been attributed to larger higher order recombination rate coefficients.[86, 87]

We can compare the properties of carriers both as a function of the number of inorganic layers and the spacer cation. At low fluences, the value of $\phi \sum \mu_{max}$ for the $n = 1$ BPEA compound is slightly larger than the analogous n-butylammonium (BA) Ruddlesden–Popper compound. However, we find that $\phi \sum \mu_{max}$ of $(BPEA)_2(CH_3NH_3)Pb_2I_7$ is approximately an order of magnitude higher than for $(BA)_2(CH_3NH_3)Pb_2I_7$. From the absorbance data, changes in dielectric confinement from the different L ions do not affect the energy of the excitonic absorption onset. However, the difference in the dielectric constant of BPEA compared to an alkylammonium chain could decrease the exciton binding energy, promoting increased free carrier formation. To understand the difference in the behavior, we must also consider factors related to the samples in the TRMC experiment.

The electronic properties of layered R–P phases are highly anisotropic and the details of the physical properties of the samples must be considered to understand the

TRMC results. The carrier mobilities within the Pb–I sheets (in-plane) are much higher than between subsequent Pb–I sheets (out-of-plane) because the electronic coupling between layers in R–P compounds through the L cation is weak.[55, 91, 101, 102]It is therefore important to understand the orientation of the crystals with respect to the microwave field to interpret the magnitude of the figure of merit. TRMC measurements on $n = 1$ and 2 were done on powders whereas those of $(BA)_2PbI_4$ and $(BA)_2(CH_3NH_3)Pb_2I_7$ were performed on thin films. However, these films were found to be highly textured – the phase fractions corresponding to lead iodide layers being oriented inplane (parallel to substrate surface) were $f = 1.0$ in $n = 1$ and $f = 0.75$ in $n = 2$, respectively.[86] Therefore, the thin film measurements should also yield values that are highly biased towards the in-plane mobilities. In the $(BPEA)_2PbI_4$ compound, the laser excitation consists of photons with energy (2.33 eV) slightly below the excitonic peak energy (2.4 eV) due to limitations in our experimental setup, but there is still reasonable absorbance, as shown in Fig. 2.7. This results in a small value of ϕ in both $(BPEA)_2PbI_4$ and $(BA)_2PbI_4$ since the excitation is in a region where absorbance increases steeply with energy, the latter also having an onset of 2.4 eV, making a direct comparison between the two compounds difficult. However, we do observe that the TRMC data for the BPEA $n = 1$ compound are consistently higher than that of the corresponding BA compound (Fig. 2.8). The $n = 2$ $(BPEA)_2(CH_3NH_3)Pb_2I_7$ compound on the other hand, has a much larger value of $\phi \sum \mu_{max}$ (0.19 $cm^2 V^{-1} s^{-1}$ at 4.56×1013 photons per cm^2), than the corresponding $(BA)_2(CH_3NH_3)Pb_2I_7$ at a comparable flu-

ence (0.03 $cm^2\,V^{-1}\,s^{-1}$ at 4.49×1013 photons per cm^2). It is difficult to make a direct comparison without knowing the value of ϕ, but we can speculate that the origin of the increased TRMC signal is due to decreased dielectric confinement. The majority (75%) of Pb–I sheets in $(BA)_2(CH_3NH_3)Pb_2I_7$ film are oriented in-plane, so even a powder sample of $(BPEA)_2(CH_3NH_3)Pb_2I_7$ with entirely in-plane Pb–I sheets would not solely account for the order of magnitude difference in $\phi \sum \mu_{max}$, assuming similar carrier yields and mobilities. Factors that could therefore have larger influence on this value are grain size, defect density, and the dielectric environment induced by the spacer cation. Yield-mobility products measured from TRMC can be affected by the grain size, which is $\sim\mu$m scale for the BPEA powders and was $\sim$100 nm in the BA films, however, this effect has been shown to be minimal above 100 nm in $CH_3NH_3PbI_3$.[103] Slower solvothermal crystal growth could result in BPEA crystals with a lower defect concentration than faster growth during spin-coating of the BA thin films, but the monotonic increase in $\phi \sum \mu_{max}$ with decreasing laser fluence suggests comparable recombination rate constants.[86] The increased TRMC signal in both BPEA compounds can be attributed to increased charge screening effects due to a larger dielectric constant, allowing easier dissociation of excitons into free carriers. This difference in the effective dielectric environment could also influence carrier mobility within the lead iodide sheets, accounting for some of the increase. Therefore, when considering all the factors affecting $\phi \sum \mu_{max}$, it appears that the use of aromatic ammonium cations improves carrier transport relative to that of a straight alkyl chain. Our result suggests that us-

ing a higher dielectric constant group in the spacer molecule in Ruddlesden–Popper compounds can improve the overall transport properties.

Bibliography

[1] Energy Information Administration (US) and Government Publications Office. *International Energy Outlook 2023*. Government Printing Office, 2023.

[2] The Energy Institute. *Statistical Review of World Energy*. 72nd ed., The Energy Institute, 2023.

[3] P.A. Arias, N. Bellouin, E. Coppola, R.G. Jones, G. Krinner, J. Marotzke, V. Naik, M.D. Palmer, G.-K. Plattner, J. Rogelj, M. Rojas, J. Sillmann, T. Storelvmo, P.W. Thorne, B. Trewin, K. Achuta Rao, B. Adhikary, R.P. Allan, K. Armour, G. Bala, R. Barimalala, S. Berger, J.G. Canadell, C. Cassou, A. Cherchi, W. Collins, W.D. Collins, S.L. Connors, S. Corti, F. Cruz, F.J. Dentener, C. Dereczynski, A. Di Luca, A. Diongue Niang, F.J. Doblas-Reyes, A. Dosio, H. Douville, F. Engelbrecht, V. Eyring, E. Fischer, P. Forster, B. Fox-Kemper, J.S. Fuglestvedt, J.C. Fyfe, N.P. Gillett, L. Goldfarb, I. Gorodetskaya, J.M. Gutierrez, R. Hamdi, E. Hawkins, H.T. Hewitt, P. Hope, A.S. Islam, C. Jones, D.S. Kaufman, R.E. Kopp, Y. Kosaka, J. Kossin, S. Krakovska, J.-Y. Lee, J. Li, T. Mauritsen, T.K. Maycock, M. Meinshausen, S.-K. Min, P.M.S. Monteiro, T. Ngo-Duc, F. Otto, I. Pinto, A. Pirani, K. Raghavan, R. Ranasinghe, A.C. Ruane, L. Ruiz, J.-B. Sallée, B.H. Samset, S. Sathyendranath, S.I. Seneviratne, A.A. Sörensson, S. Szopa, I. Takayabu, A.-M. Tréguier, B. van den Hurk, R. Vautard, K. von Schuckmann, S. Zaehle,

X. Zhang, K. Zickfeld, V. Masson-Delmotte, P. Zhai, A. Pirani, S.L. Connors, C. Péan, S. Berger, N. Caud, Y. Chen, L. Goldfarb, M.I. Gomis, M. Huang, K. Leitzell, E. Lonnoy, J.B.R. Matthews, T.K. Maycock, T. Waterfield, O. Yelekçi, R. Yu, and B. Zhou. *Technical Summary in Climate Change 2021: The Physical Science Basis. Contribution of Working Group I to the Sixth Assessment Report of the Intergovernmental Panel on Climate Change*, pages 33–144. Cambridge University Press, Cambridge, United Kingdom and New York, NY, USA, 2021.

[4] Global Monitoring Laboratory. *THE NOAA ANNUAL GREENHOUSE GAS INDEX (AGGI)*. https://gml.noaa.gov/aggi/aggi.html, 2023. Accessed: 01/30/2024.

[5] D. J. Davidson. Exnovating for a renewable energy transition. *Nat. Energy*, 4(4):254–256, 2019.

[6] J.-P. Correa-Baena, M. Saliba, T. Buonassisi, M. Grätzel, A. Abate, W. Tress, and A. Hagfeldt. Promises and challenges of perovskite solar cells. *Science*, 358(6364):739–744, 2017.

[7] C.J. Xiao, C.Q. Jin, and X.H. Wang. Crystal structure of dense nanocrystalline $BaTiO_3$ ceramics. *Mater. Chem. Phys.*, 111(2-3):209–212, 2008.

[8] H. L. Wells. Über die cäsium-und kalium-bleihalogenide. *Zeitschrift für anorganische Chemie*, 3(1):195–210, 1893.

[9] V. M. Goldschmidt. Die gesetze der krystallochemie. *Naturwissenschaften*, 14(21):477–485, 1926.

[10] H. D. Megaw. Crystal Structure of Barium Titanate. *Nature*, 155(3938):484–485, 1945.

[11] Helen D Megaw and CNW Darlington. Geometrical and structural relations in the rhombohedral perovskites. *Acta Crystallographica Section A: Crystal Physics, Diffraction, Theoretical and General Crystallography*, 31(2):161–173, 1975.

[12] H. D. Megaw. Origin of ferroelectricity in barium titanate and other perovskite-type crystals. *Acta Crystallogr.*, 5(6):739–749, 1952.

[13] D. Weber. $CH_3NH_3PbX_3$, ein Pb (II)-System mit kubischer perowskitstruktur/$CH_3NH_3PbX_3$, a Pb (II)-System with Cubic Perovskite Structure. *ZNB*, 33(12):1443–1445, 1978.

[14] A. Kojima, K. Teshima, Y. Shirai, and T. Miyasaka. Organometal Halide Perovskites as Visible-Light Sensitizers for Photovoltaic Cells. *J. Am. Chem. Soc.*, 131(17):6050–6051, 2009.

[15] I. Chung, B. Lee, J. He, R. P.H. Chang, and M. G. Kanatzidis. All-solid-state dye-sensitized solar cells with high efficiency. *Nature*, 485(7399):486–489, 2012.

[16] M. M. Lee, J. Teuscher, T. Miyasaka, T. N. Murakami, and H. J. Snaith. Effi-

cient Hybrid Solar Cells Based on Meso-Superstructured Organometal Halide Perovskites. *Science*, 338(6107):643–647, 2012.

[17] H.-S. Kim, C.-R. Lee, J.-H. Im, K.-B. Lee, T. Moehl, A. Marchioro, S.-J. Moon, R. Humphry-Baker, J.-H. Yum, J. E. Moser, M. Grätzel, and N.-G. Park. Lead iodide perovskite sensitized all-solid-state submicron thin film mesoscopic solar cell with efficiency exceeding 9%. *Sci. Reps.*, 2(1):591, 2012.

[18] S. M. Park, M. Wei, J. Xu, H. R. Atapattu, F. T. Eickemeyer, K. Darabi, L. Grater, Y. Yang, C. Liu, S. Teale, B. Chen, T. Want, L. Zeng, A. Maxwell, Z. Wang, K. R. Rao, Z. Cai, J. T. Zakeeruddin, S. M.and Pham, C. M. Risko, A. Emassian, M. G. Kanatzidis, K. R. Graham, M. Grätzel, and E. H. Sargent. Engineering ligand reactivity enables high-temperature operation of stable perovskite solar cells. *Science*, 381(6654):209–215, 2023.

[19] B. L. Smith, M. Woodhouse, K. A.W. Horowitz, T. J. Silverman, J. Zuboy, and R. M. Margolis. Photovoltaic (PV) module technologies: 2020 benchmark costs and technology evolution framework results. Technical report, National Renewable Energy Lab.(NREL), Golden, CO (United States), 2021.

[20] G. Divitini, S. Cacovich, F. Matteocci, L. Cinà, A. Di Carlo, and C. Ducati. *In situ* observation of heat-induced degradation of perovskite solar cells. *Nat. Energy*, 1(2):1–6, 2016.

[21] E. Mosconi, J. M. Azpiroz, and F. De Angelis. *Ab Initio* Molecular Dynamics

Simulations of Methylammonium Lead Iodide Perovskite Degradation by Water. *Chem. Mater.*, 27(13):4885–4892, 2015.

[22] Y. Li, X. Xu, C. Wang, B. Ecker, J. Yang, J. Huang, and Y. Gao. Light-Induced Degradation of $CH_3NH_3PbI_3$ Hybrid Perovskite Thin Film. *J. Phys. Chem. C*, 121(7):3904–3910, 2017.

[23] N. Aristidou, I. Sanchez-Molina, T. Chotchuangchutchaval, M. Brown, L. Martinez, T. Rath, and S. A. Haque. The Role of Oxygen in the Degradation of Methylammonium Lead Trihalide Perovskite Photoactive Layers. *Angew. Chem.*, 127(28):8326–8330, 2015.

[24] T. A. Berhe, W.-N. Su, C.-H. Chen, C.-J. Pan, J.-H. Cheng, H.-M. Chen, M.-C. Tsai, A. A. Chen, L.-Y.and Dubale, and B.J. Hwang. Organometal halide perovskite solar cells: degradation and stability. *Energy Environ.*, 9(2):323–356, 2016.

[25] X. Zhao and N.-G. Park. Stability Issues on Perovskite Solar Cells. *Photonics*, 2(4):1139–1151, 2015.

[26] K. S. Aleksandrov. Structural phase transitions in layered perovskitelike crystals. *Crystallogr. Rep.*, 40(2), 1995.

[27] J. Even, L. Pedesseau, and C. Katan. Understanding Quantum Confinement of Charge Carriers in Layered 2D Hybrid Perovskites. *ChemPhysChem*, 15(17):3733–3741, 2014.

[28] S. Gharibzadeh, B. Abdollahi Nejand, M. Jakoby, T. Abzieher, D. Hauschild, S. Moghadamzadeh, J. A. Schwenzer, P. Brenner, R. Schmager, and A. A. Haghighirad. Record open-circuit voltage wide-bandgap perovskite solar cells utilizing 2D/3D perovskite heterostructure. *Adv. Energy Mater.*, 9(21):1803699, 2019.

[29] N. M. Haegel, P. Verlinden, M. Victoria, P. Altermatt, H. Atwater, T. Barnes, C. Breyer, C. Case, S. De Wolf, and C. Deline. Photovoltaics at multi-terawatt scale: waiting is not an option. *Science*, 380(6640):39–42, 2023.

[30] L. Chu, S. Zhai, W. Ahmad, J. Zhang, Y. Zang, W. Yan, and Y. Li. High-performance large-area perovskite photovoltaic modules. *Nano Res. Energy*, 1(2):e9120024, 2022.

[31] G. Eder, G. Peharz, R. Trattnig, P. Bonomo, E. Saretta, F. Frontini, C. S. Polo López, H. R. Wilson, J. Eisenlohr, N. M. Chivelet, S. Karlson, N. Jakica, and A. Zanelli. COLOURED BIPV: Market, Research and Development, 2019.

[32] N.-G. Park and K. Zhu. Scalable fabrication and coating methods for perovskite solar cells and solar modules. *Nat. Rev. Mater.*, 5(5):333–350, 2020.

[33] P. Zhu, C. Chen, J. Dai, Y. Zhang, R. Mao, S. Chen, J. Huang, and J. Zhu. Towards the Commercialization of Perovskite Solar Modules. *Adv. Mater.*, page 2307357, 2024.

[34] G. A. Papavassiliou, G. C. Mousdis and I. B. Koutselas. Some New Organic–Inorganic Hybrid Semiconductors Based on Metal Halide Units: Structural, Optical and Related Properties. *Adv. Mater. Opt. Electron.*, 9(6):265–271, 1999.

[35] B. Saparov and D. B. Mitzi. Organic–Inorganic Perovskites: Structural Versatility for Functional Materials Design. *Chem. Rev.*, 116(7):4558–4596, 2016.

[36] J. Berry, T. Buonassisi, D. A. Egger, G. Hodes, L. Kronik, Y.-L. Loo, I. Lubomirsky, S. R. Marder, Y. Mastai, J. S. Miller, D. B. Mitzi, Y. Paz, A. M. Rappe, I. Riess, B. Rybtchinski, O. Stafsudd, V. Stevanovic, M. F. Toney, D. Zitoun, A. Kahn, D. Ginley, and D. Cahen. Hybrid Organic–Inorganic Perovskites (HOIPs): Opportunities and Challenges. *Adv. Mater.*, 27(35):5102–5112, 2015.

[37] W. Zhang, G. E. Eperon, and H. J. Snaith. Metal halide perovskites for energy applications. *Nat. Energy*, 1(6):16048, 2016.

[38] D. B. Mitzi, K. Chondroudis, and C. R. Kagan. Organic–inorganic electronics. *IBM J. Res. Dev.*, 45(1):29–45, 2001.

[39] D. B. Mitzi, L. L. Kosbar, C. E. Murray, M. Copel, and A. Afzali. High-mobility ultrathin semiconducting films prepared by spin coating. *Nature*, 428(6980):299–303, 2004.

[40] D. B. Mitzi, C. A. Feild, W. T. A. Harrison, and A. M. Guloy. Conducting tin halides with a layered organic-based perovskite structure. *Nature*, 369(6480):467–469, 1994.

[41] NREL. Best Research-Cell Efficiencies. https://www.nrel.gov/pv/assets/pdfs/best-research-cell-efficiencies.pdf, 2023. Accessed: December 2023.

[42] M. A. Green, E. D. Dunlop, M. Yoshita, N. Kopidakis, K. Bothe, G. Siefer, and X. Hao. Solar cell efficiency tables (Version 63). *Prog. Photovolt: Res. Appl*, 2024.

[43] M. Nakamura, K. Yamaguchi, Y. Kimoto, Y. Yasaki, T. Kato, and H. Sugimoto. Cd-Free Cu(In,Ga)(Se,S)$_2$ Thin-Film Solar Cell With Record Efficiency of 23.35%. *J-PV*, 9(6):1863–1867, 2019.

[44] M. Yuan, L. N. Quan, R. Comin, G. Walters, R. Sabatini, O. Voznyy, S. Hoogland, Y. Zhao, E. M. Beauregard, P. Kanjanaboos, Z. Lu, D. H. Kim, and E. H. Sargent. Perovskite energy funnels for efficient light-emitting diodes. *Nat. Nanotechnol.*, 11(10):872–877, 2016.

[45] N. Wang, L. Cheng, R. Ge, S. Zhang, Y. Miao, W. Zou, C. Yi, Y. Sun, Y. Cao, and R. and Yang. Perovskite light-emitting diodes based on solution-processed self-organized multiple quantum wells. *Nat. Photonics*, 10(11):699–704, 2016.

[46] K. Lin, J. Xing, L. N. Quan, F. P. G. de Arquer, X. Gong, J. Lu, L. Xie, W. Zhao, D. Zhang, C Yan, W. Li, X. Liu, Y. Lu, J. Kirman, E. H. Sargent, Q. Xiong, and S. Wei. Perovskite light-emitting diodes with external quantum efficiency exceeding 20 per cent. *Nature*, 562(7726):245–248, 2018.

[47] Z. Xiao, R. A. Kerner, L. Zhao, N. L. Tran, K. M. Lee, T.-W. Koh, G. D. Scholes, and B. P. Rand. Efficient perovskite light-emitting diodes featuring nanometre-sized crystallites. *Nat. Photonics*, 11(2):108–115, 2017.

[48] M. V. Kovalenko, L Protesescu, and M. I. Bodnarchuk. Properties and potential optoelectronic applications of lead halide perovskite nanocrystals. *Science*, 358(6364):745–750, 2017.

[49] L. Protesescu, S. Yakunin, M. I. Bodnarchuk, F. Krieg, R. Caputo, C. H. Hendon, R. X. Yang, A. Walsh, and M. V. Kovalenko. Nanocrystals of Cesium Lead Halide Perovskites ($CsPbX_3$, X= Cl, Br, and I): Novel Optoelectronic Materials Showing Bright Emission with Wide Color Gamut. *Nano Lett.*, 15(6):3692–3696, 2015.

[50] M. C. Weidman, A. J. Goodman, and W. A. Tisdale. Colloidal Halide Perovskite Nanoplatelets: An Exciting New Class of Semiconductor Nanomaterials. *Chem. Mater.*, 29(12):5019–5030, 2017.

[51] M. D. Smith and H. I. Karunadasa. White-Light Emission from Layered Halide Perovskites. *Acc. Chem. Res.*, 51(3):619–627, 2018.

[52] M. D. Smith, A. Jaffe, E. R. Dohner, A. M. Lindenberg, and H. I. Karunadasa. Structural origins of broadband emission from layered Pb–Br hybrid perovskites. *Chem. Sci.*, 8(6):4497–4504, 2017.

[53] R. M. Kennard, C. J. Dahlman, H. Nakayama, R. A. DeCrescent, J. A. Schuller, R. Seshadri, K. Mukherjee, and M. L. Chabinyc. Phase Stability and Diffusion

in Lateral Heterostructures of Methyl Ammonium Lead Halide Perovskites. *ACS Appl. Mat. Interfaces*, 11(28):25313–25321, 2019.

[54] I. C. Smith, E. T. Hoke, D. Solis-Ibarra, M. D. McGehee, and H. I. Karunadasa. A Layered Hybrid Perovskite Solar-Cell Absorber with Enhanced Moisture Stability. *Angew. Chem.*, 53(42):11232–11235, 2014.

[55] H. Tsai, W. Nie, J.-C. Blancon, C. C. Stoumpos, R. Asadpour, B. Harutyunyan, A. J. Neukirch, R. Verduzco, J. J. Crochet, S. Tretiak, L. Pedesseau, J. Even, M. A. Alam, G. Gupta, J. Lou, P. M. Ajayan, M. J. Bedzky, M. J. Kanatzidis, and A. D. Hohite. High-efficiency two-dimensional Ruddlesden–Popper perovskite solar cells. *Nature*, 536(7616):312–316, 2016.

[56] L. Pedesseau, D. Sapori, B. Traore, R. Robles, H.-H. Fang, M. A. Loi, H. Tsai, W. Nie, J.-C. Blancon, A. Neukirch, S. Tretiak, A. D. Mohite, C. Katan, J. Eve, and M. Kepenekian. Advances and Promises of Layered Halide Hybrid Perovskite Semiconductors. *ACS Nano*, 10(11):9776–9786, 2016.

[57] X. Zhang, G. Wu, S. Yang, W. Fu, Z. Zhang, C. Chen, W. Liu, J. Yan, W. Yang, and H. Chen. Vertically Oriented 2D Layered Perovskite Solar Cells with Enhanced Efficiency and Good Stability. *Small*, 13(33):1700611, 2017.

[58] S. N. Ruddlesden and P. Popper. New compounds of the K_2NiF_4 type. *Acta Crystallogr.*, 10(8):538–539, 1957.

[59] S. N. Ruddlesden and P. Popper. The compound $Sr_3Ti_2O_7$ and its structure. *Acta Crystallogr.*, 11(1):54–55, 1958.

[60] Y. Chen, Y. Sun, J. Peng, J. Tang, K. Zheng, and Z. Liang. 2D Ruddlesden–Popper Perovskites for Optoelectronics. *Adv. Mater.*, 30(2):1703487, 2018.

[61] Y. Chen, S. Yu, Y. Sun, and Z. Liang. Phase Engineering in Quasi-2D Ruddlesden–Popper Perovskites. *J. Phys. Chem. Lett.*, 9(10):2627–2631, 2018.

[62] T. M. Koh, B. Febriansyah, and N. Mathews. Ruddlesden–Popper Perovskite Solar Cells. *Chem*, 2(3):326–327, 2017.

[63] Y. Chen, Y. Sun, J. Peng, W. Zhang, X. Su, K. Zheng, T. Pullerits, and Z. Liang. Tailoring Organic Cation of 2D Air-Stable Organometal Halide Perovskites for Highly Efficient Planar Solar Cells. *Adv. Energy Mater.*, 7(18):1700162, 2017.

[64] Y. Liu, S. Akin, L. Pan, R. Uchida, N. Arora, J. V. Milić, A. Hinderhofer, F. Schreiber, A. R. Uhl, S. M. Zakeeruddin, A. Haffeldt, M. I. Dar, and M. Grätzel. Ultrahydrophobic 3D/2D fluoroarene bilayer-based water-resistant perovskite solar cells with efficiencies exceeding 22%. *Science advances*, 5(6):eaaw2543, 2019.

[65] Z. Wang, Q. Lin, F. P Chmiel, N. Sakai, L. M. Herz, and H. J. Snaith. Efficient ambient-air-stable solar cells with 2D–3D heterostructured butylammonium-caesium-formamidinium lead halide perovskites. *Nat. Energy*, 2(9):1–10, 2017.

[66] J.-W. Lee, Z. Dai, T.-H. Han, C. Choi, S.-Y. Chang, S.-J. Lee, N. De Marco, H. Zhao, P. Sun, Y. Huang, and Y. Yang. 2D perovskite stabilized phase-pure formamidinium perovskite solar cells. *Nat. Commun.*, 9(1):3021, 2018.

[67] R. Hamaguchi, M. Yoshizawa-Fujita, T. Miyasaka, H. Kunugita, K. Ema, Y. Takeoka, and M. Rikukawa. Formamidine and cesium-based quasi-two-dimensional perovskites as photovoltaic absorbers. *Chem. Commun.*, 53(31):4366–4369, 2017.

[68] D. Yu, F. Cao, Y. Shen, X. Liu, Y. Zhu, and H.. Zeng. Dimensionality and Interface Engineering of 2D Homologous Perovskites for Boosted Charge-Carrier Transport and Photodetection Performances. *J. Phys. Chem. Lett.*, 8(12):2565–2572, 2017.

[69] M. C. Weidman, M. Seitz, S. D. Stranks, and W. A. Tisdale. Highly Tunable Colloidal Perovskite Nanoplatelets through Variable Cation, Metal, and Halide Composition. *ACS nano*, 10(8):7830–7839, 2016.

[70] Z. Chen, C. Zhang, X.-F. Jiang, M. Liu, R. Xia, T. Shi, D. Chen, Q. Xue, Y.-J. Zhao, S. Su, H-L. Yip, and Y. Cao. High-Performance Color-Tunable Perovskite Light Emitting Devices through Structural Modulation from Bulk to Layered Film. *Adv. Mater.*, 29(8):1603157, 2017.

[71] K.-Z. Du, Q. Tu, X. Zhang, Q. Han, J. Liu, S. Zauscher, and D. B. Mitzi. Two-Dimensional Lead (II) Halide-Based Hybrid Perovskites Templated by Acene

Alkylamines: Crystal Structures, Optical Properties, and Piezoelectricity. *Inorg. Chem.*, 56(15):9291–9302, 2017.

[72] D. B. Mitzi. Templating and structural engineering in organic–inorganic perovskites. *J. Chem. Soc., Dalton Trans.*, (1):1–12, 2001.

[73] D. B. Mitzi, K. Chondroudis, and C. R. Kagan. Design, Structure, and Optical Properties of OIrganic–Inorganic Perovskites Containing an Oligothiophene Chromophore. *Inorg. Chem.*, 38(26):6246–6256, 1999.

[74] R. L. Milot, R. J. Sutton, G. E. Eperon, A. A. Haghighirad, J. Martinez Hardigree, L. Miranda, H. J. Snaith, M. B. Johnston, and L. M. Herz. Charge-Carrier Dynamics in 2D Hybrid Metal–Halide Perovskites. *Nano Lett.*, 16(11):7001–7007, 2016.

[75] L. Mao, W. Ke, L. Pedesseau, Y. Wu, C. Katan, J. Even, M. R. Wasielewski, C. C. Stoumpos, and M. G. Kanatzidis. Hybrid Dion–Jacobson 2D Lead Iodide Perovskites. *J. Am. Chem. Soc.*, 140(10):3775–3783, 2018.

[76] Y. Li, J. V. Milić, A. Ummadisingu, J.-Y. Seo, J.-H. Im, H.S. Kim, Y. Liu, M. I. Dar, S. M. Zakeeruddin, P. Wang, A. Hafgeldt, and Grätzel. Bifunctional Organic Spacers for Formamidinium-Based Hybrid Dion–Jacobson Two-Dimensional Perovskite Solar Cells. *Nano Lett.*, 19(1):150–157, 2018.

[77] J. A. Sichert, Y. Tong, N. Mutz, M. Vollmer, S. Fischer, K. Z. Milowska, R. García Cortadella, B. Nickel, C. Cardenas-Daw, J. K. Stolarczyk, A. S. Ur-

ban, and J. Feldmann. Quantum Size Effect in Organometal Halide Perovskite Nanoplatelets. *Nano Lett.*, 15(10):6521–6527, 2015.

[78] G. M. Sheldrick. SADABS, program for scaling and correction of area detector data. *University of Göttingen, Germany*, 1996.

[79] G.M. Sheldrick. SHELXTL v. 6.12, structure determination software suite, 2000.

[80] H. Hauptman. Phasing methods for protein crystallography. *Curr. Opin. Struct. Biol.*, 7(5):672–680, 1997.

[81] K. Momma and F. Izumi. VESTA 3 for three-dimensional visualization of crystal, volumetric and morphology data. *J. Appl. Crystallogr.*, 44(6):1272–1276, 2011.

[82] B. H. Toby and R. B. Von Dreele. GSAS-II: the genesis of a modern open-source all purpose crystallography software package. *J. Appl. Crystallogr.*, 46(2):544–549, 2013.

[83] Brian H Toby. EXPGUI, a graphical user interface for GSAS. *J. Appl. Crystallogr.*, 34(2):210–213, 2001.

[84] W. A. Dollase. Correction of Intensities for Preferred Orientation in Powder Diffractometry: Application of the March Model. *J. Appl. Crystallogr.*, 19(4):267–272, 1986.

[85] P. Kubelka and F. Munk. An article on optics of paint layers. *Z. Tech. Phys*, 12(593-601):259–274, 1931.

[86] N. R. Venkatesan, J. G. Labram, and M. L. Chabinyc. Charge-Carrier Dynamics and Crystalline Texture of Layered Ruddlesden–Popper Hybrid Lead Iodide Perovskite Thin Films. *ACS Energy Lett.*, 3(2):380–386, 2018.

[87] J. G. Labram, N. R. Venkatesan, C. J. Takacs, H. A. Evans, E. E. Perry, F. Wudl, and M. L. Chabinyc. Charge transport in a two-dimensional hybrid metal halide thiocyanate compound. *J. Mater. Chem. C*, 5(24):5930–5938, 2017.

[88] J. G. Labram and M. L. Chabinyc. Recombination at high carrier density in methylammonium lead iodide studied using time-resolved microwave conductivity. *J. Appl. Phys.*, 122(6), 2017.

[89] T. J. Savenije, A. J. Ferguson, N. Kopidakis, and G. Rumbles. Revealing the Dynamics of Charge Carriers in Polymer: Fullerene Blends Using Photoinduced Time-Resolved Microwave Conductivity. *J. Phys. Chem. C*, 117(46):24085–24103, 2013.

[90] J. Calabrese, N.L. Jones, R.L. Harlow, N. Herron, D.L. Thorn, and Y. Wang. Preparation and Characterization of Layered Lead Halide Compounds. *J. Am. Chem. Soc.*, 113(6):2328–2330, 1991.

[91] C. C. Stoumpos, D. H. Cao, D. J. Clark, J. Young, J. M. Rondinelli, J. I. Jang, J. T. Hupp, and M. G. Kanatzidis. Ruddlesden–Popper Hybrid Lead Iodide Perovskite 2D Homologous Semiconductors. *Chem. Mater.*, 28(8):2852–2867, 2016.

[92] G. Grancini, C. Roldán-Carmona, I. Zimmermann, E. Mosconi, X. Lee, D. Martineau, S. Narbey, F. Oswald, F. De Angelis, M. Graetzel, and M. K. Nazeeruddin. One-Year stable perovskite solar cells by 2D/3D interface engineering. *Nature Commun.*, 8(1):15684, 2017.

[93] H. Oga, A. Saeki, Y. Ogomi, S. Hayase, and S. Seki. Improved Understanding of the Electronic and Energetic Landscapes of Perovskite Solar Cells: High Local Charge Carrier Mobility, Reduced Recombination, and Extremely Shallow Traps. *J. Am. Chem. Soc.*, 136(39):13818–13825, 2014.

[94] T. J. Savenije, C. S. Ponseca Jr, L. Kunneman, M. Abdellah, K. Zheng, Y. Tian, Q. Zhu, S. E. Canton, I. G. Scheblykin, T. Pullerits, A. Yartsev, and V. Sundström. Thermally Activated Exciton Dissociation and Recombination Control the Carrier Dynamics in Organometal Halide Perovskite. *J. Phys. Chem. Lett.*, 5(13):2189–2194, 2014.

[95] E. M. Hutter, M. C. Gélvez-Rueda, A. Osherov, V. Bulović, F. C. Grozema, S. D. Stranks, and T. J. Savenije. Direct–indirect character of the bandgap in methylammonium lead iodide perovskite. *Nat. Mater.*, 16(1):115–120, 2017.

[96] C. S. Ponseca Jr, T. J. Savenije, M. Abdellah, K. Zheng, A. Yartsev, T. Pascher, T. Harlang, P. Chabera, T. Pullerits, A. Stepanov, J.-P. Wolf, and V. Sundstöm. Organometal Halide Perovskite Solar Cell Materials Rationalized: Ultrafast

Charge Generation, High and Microsecond-Long Balanced Mobilities, and Slow Recombination. *J. Am. Chem. Soc.*, 136(14):5189–5192, 2014.

[97] R. Brenes, D. Guo, A. Osherov, N. K. Noel, C. Eames, E. M. Hutter, S. K. Pathak, F. Niroui, R. H. Friend, M. S. Islam, H. J. Snaith, V. Bulovi, Savenije. T. J., and S. D. Stranks. Metal Halide Perovskite Polycrystalline Films Exhibiting Properties of Single Crystals. *Joule*, 1(1):155–167, 2017.

[98] Y. Hu, E. M. Hutter, P. Rieder, I. Grill, J. Hanisch, M. F. Aygüler, A. G. Hufnagel, M. Handloser, T. Bein, A. Hartschuh, K. Tvingstedt, V. Dyakonov, A. Baumann, T. J. Savenije, M. L. Petrus, and P. Docampo. Understanding the Role of Cesium and Rubidium Additives in Perovskite Solar Cells: Trap States, Charge Transport, and Recombination. *Adv. Energy Meter.*, 8(16):1703057, 2018.

[99] M. Abdi-Jalebi, Z. Andaji-Garmaroudi, S. Cacovich, C. Stavrakas, B. Philippe, J. M. Richter, M. Alsari, E. P. Booker, E. M. Hutter, A. J. Pearson, S. Lilliu, T. J. Savenije, H. Rensmo, C. Divitini, G. Ducati, R. H. Friend, and S. D. Stranks. Maximizing and stabilizing luminescence from halide perovskites with potassium passivation. *Nature*, 555(7697):497–501, 2018.

[100] O. G. Reid, D. T. Moore, Z. Li, D. Zhao, Y. Yan, K. Zhu, and G. Rumbles. Quantitative analysis of time-resolved microwave conductivity data. *J. Phys. D: Appl. Phys.*, 50(49):493002, 2017.

[101] S. Silver, J. Yin, H. Li, J.-L. Brédas, and A. Kahn. Characterization of the Valence

and Conduction Band Levels of $n = 1$ 2D Perovskites: a Combined Experimental and Theoretical Investigation. *Adv. Energy Mater*, 8(16):1703468, 2018.

[102] D. B. Straus and C. R. Kagan. Electrons, Excitons, and Phonons in Two-Dimensional Hybrid Perovskites: Connecting Structural, Optical, and Electronic Properties. *J. Phys. Chem. Lett.*, 9(6):1434–1447, 2018.

[103] O. G. Reid, M. Yang, N. Kopidakis, K. Zhu, and G. Rumbles. Grain-Size-Limited Mobility in Methylammonium Lead Iodide Perovskite Thin Films. *ACS Energy Lett.*, 1(3):561–565, 2016.